PHYSICAL REVIEW B **87**, 054509 (2013)

Transport in multiterminal superconductor/ferromagnet junctions having spin-dependent interfaces

Kuei Sun,[1] Nayana Shah,[1] and Smitha Vishveshwara[2]
[1]*Department of Physics, University of Cincinnati, Cincinnati, Ohio 45221-0011, USA*
[2]*Department of Physics, University of Illinois at Urbana-Champaign, Urbana, Illinois 61801-3080, USA*
(Received 20 September 2012; published 22 February 2013)

We study electronic transport in junctions consisting of a superconductor electrode and two ferromagnet (F) leads in which crossed Andreev reflections (CAR) and elastic cotunnelings are accommodated. We model the system using an extended Blonder-Tinkham-Klapwijk treatment with a key modification that accounts for spin-dependent interfacial barriers (SDIB). We compute current-voltage relations as a function of parameters characterizing the SDIB, magnetization in the F leads, geometry of the junction, and temperature. Our results reveal a rich range of significantly altered physics due to a combination of interfering spin-dependent scattering processes and population imbalance in the ferromagnets, such as a significant enhancement in CAR current and a sign change in the relative difference between resistance of two cases having a antiparallel or parallel alignment of the magnetization in the F leads, respectively. Our model accounts for the surprising experimental findings of positive relative resistance by M. Colci *et al.* [Phys. Rev. B **85**, 180512(R) (2012)] as well as previously measured negative relative resistance results, both within sufficiently large parameter regions.

DOI: 10.1103/PhysRevB.87.054509 PACS number(s): 74.45.+c, 73.23.−b, 74.25.fc, 72.25.−b

I. INTRODUCTION

Over the past decades, extensive theoretical and experimental research has focused on electronic transport in superconductor–normal metal (S-N) heterostructures, wherein conducting electrons propagate through bulk materials and scatter at interfaces.[1–4] More recently, attention has turned to systems comprising an S electrode in contact with multi-N terminals, in which a unique scattering process known as the crossed Andreev reflection (CAR) can occur.[5–15] The CAR process involves an electron in an N terminal impinging the S accompanied by a hole of opposite spin reflecting in another N terminal separated within the superconducting coherence length, and generating a Cooper pair in S. The nonlocal and coherent nature of CAR makes such a device a platform for exploring quantum entanglement, providing potential application to quantum computing.[16]

Another avenue of S-N junction studies which has recently gained prominence is the presence of ferromagnetic order in the normal system. Transport physics can be significantly altered when the normal system is a ferromagnet (F). For instance, the F bulk can be created by spin imbalance, changing the populations involved in the transport processes as well as spin-dependent interfaces that modify both the proximity effect[17–20] and electron scattering.[21–24] In S-F junctions, the interplay between ferromagnetic and superconducting orders around the interface strongly affects Andreev reflections[25–29] (the direct process of an incoming electron reflecting as a hole of opposite spin within the same terminal[30]), while in S-F-S systems it can lead to Josephson π junctions sustaining negative critical currents.[31–34]

Recent experiments[35–38] have been performed on S-FF-S devices in which two F bridges are both laid across two S electrodes, with the separation between the two F bridges being smaller than the superconducting coherence length (thus capable of accommodating CAR). The results show that the system can exhibit both positive[37,38] and negative[35,36] relative resistances between two different cases characterized by an antiparallel (AP) or parallel (P) alignment of magnetization in the F leads, respectively. [The relative resistance, denoted by δR, is defined as the normalized value of the difference $R_{\mathrm{AP}} - R_{\mathrm{P}}$, where $R_{\mathrm{AP(P)}}$ is the resistance across the junction with AP (P) configuration. See Eq. (29) for details.] Since coherent transport between the two S electrodes is not revealed in the experimental data, the S-FF-S device can be considered as a series connection of two independent S-FF junctions (each of which, as illustrated in Fig. 1, carries coherent transport between the two F leads). Therefore, one can study the transport properties of the S-FF-S system by investigating the S-FF junction. In such cases, the negative δR ($R_{\mathrm{P}} > R_{\mathrm{AP}}$) can be understood by an intuitive picture that the suppression of CAR due to spin imbalance raises the resistance of the P case, or can be explicitly explained by a Blonder-Tinkham-Klapwijk (BTK) treatment[1] with spin-independent interfacial barriers.[39] However, such a BTK model cannot explain the counterintuitive data of positive δR, which suggests that a competitive effect should be incorporated.

Motivated by these experiments, we provide one of the first comprehensive theoretical studies of S-FF junctions having spin-dependent interfacial barriers (SDIB). The presence of SDIB at the junction between a superconductor and a single ferromagnet has been shown to considerably alter transport properties.[21–29] For our situation, the SDIB plays a prominent role in affecting coherence and cross correlations between excitations in the two ferromagnets. We explore the large parameter space of the system and show that SDIB can give rise to a rich range of physics depending on the choice of parameters. We provide a consistent scenario explaining both competing experimental results described above. In fact, a small subsection of the studies investigated here has been directly employed to explain the counterintuitive experimental results presented in Ref. 38. We propose a microscopic picture describing the SDIB within an extended BTK model and compute transport properties of the system as a function of the derived SDIB parameters. We carefully discuss the various scattering processes responsible for the difference in behavior

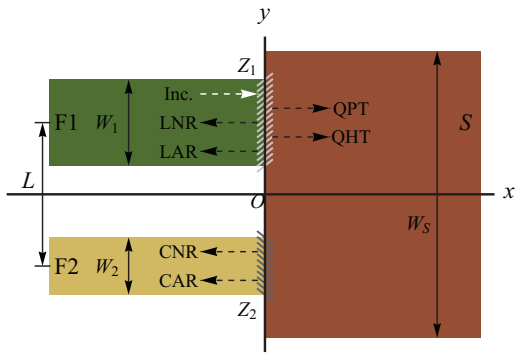

FIG. 1. (Color online) Cartoon representation of an SFF junction. The system has two ferromagnetic leads F1 (F2), illustrated as the shaded regions in the second (third) quadrant having width $W_{1(2)}$ and separation L between them, and a superconducting electrode S illustrated as the shaded region in the $x > 0$ plane with width W_S. The F1(2)-S interfaces (twilled regions) are described by spin-dependent interface parameters Z_1 and Z_2, respectively. Black dashed arrows indicate six scattering processes experienced by an electron in F1 incident on the interface (Inc., white dashed arrow): local normal reflection (LNR), local Andreev reflection (LAR), crossed normal reflection (CNR, also referred to as elastic cotunneling), crossed Andreev reflection (CAR), quasiparticle transmission (QPT), and quasihole transmission (QHT).

between the P and AP cases and show that interference between these processes can play a significant role. We analyze transport properties as a function of magnetization, the geometry of the system, and temperature. We show that they reveal several interesting features, such as the sought-after differing behavior for the P and AP cases, oscillations as a function of geometry, and, under certain conditions, enhancement of crossed Andreev reflection, which would be indicative of long-range entanglement.

Our studies thus not only reconcile the apparently conflicting results of the various experiments; they also provide several other aspects to explore within the same experimental settings. Our extended BTK model also applies to several other possible experimental geometries, including other multiterminal superconducting hybrids that possess a two-dimensional nature characterizing the elongation and separation of the terminals, such as multilayer[40–42] or multiwire[43,44] devices in the presence of the spin-dependent interfacial scattering.

The paper is outlined as follows. In Sec. II we model the geometry of the system and present the corresponding Hamiltonian describing six scattering processes. We also discuss a possible microscopic mechanism resulting in an SDIB. In Sec. III, by applying the BTK treatment we derive the current-voltage (I-V) relation as a function of exchange energy, SDIB parameters, the geometry of the junction and temperature. In Sec. IV, we illustrate data showing the dependence of transport properties on several groups of variables associated with ferromagnetism, geometry of the system, and temperature, respectively. We discuss the effects of SDIB compared to the spin-independent case and other effects competing or cooperating with SDIB. In Sec. V we summarize our results and comment on the scope of our work.

II. THE MODEL

To model our basic setup shown in Fig. 1, we consider a two-dimensional junction consisting of an S electrode in contact with two F leads. The S electrode of width W_S is located in the $x > 0$ half plane, while the two F leads (F1 and F2), of widths W_1 and W_2, respectively, are located in the $x < 0$ half plane and separated by L in the $\hat{\mathbf{y}}$ direction. This system is described by a Bogoliubov–de Gennes (BdG) Hamiltonian

$$\begin{pmatrix} H_0 - \sigma\epsilon^{\rm ex}(\mathbf{r}) + V_\sigma^{\rm I}(\mathbf{r}) & \Delta(\mathbf{r}) \\ \Delta(\mathbf{r}) & -\left[H_0 - \bar{\sigma}\epsilon^{\rm ex}(\mathbf{r}) + V_{\bar{\sigma}}^{\rm I}(\mathbf{r})\right] \end{pmatrix}. \quad (1)$$

Here $H_0 = -\frac{\hbar^2}{2m}\nabla^2 - \epsilon_F$ is the free Hamiltonian with Fermi energy ϵ_F, $\mathbf{r} = (x, y)$ denotes the coordinates, $\sigma = \pm$ denotes up (down) spin states, respectively, and $\bar{\sigma} \equiv -\sigma$. The superconducting gap Δ, exchange energy $\epsilon^{\rm ex}$, and interface potential V_I are given by

$$\Delta(\mathbf{r}) = \Delta\theta(x)\theta_S(y), \quad (2)$$

$$\epsilon^{\rm ex}(\mathbf{r}) = \theta(-x)\sum_{j=1,2}\epsilon_j^{\rm ex}\theta_j(y), \quad (3)$$

$$V_\sigma^{\rm I}(\mathbf{r}) = \delta(x)\sum_{j=1,2} Z_{j\sigma}\theta_j(y), \quad (4)$$

where $\epsilon_{j=1,2}^{\rm ex}$ are exchange energies in F1(2), respectively, indicating the Zeeman splitting between up and down spins induced by ferromagnetism. The parameter $Z_{j\sigma}$ describes the corresponding S-F interfacial barrier, θ is the step function, and

$$\theta_j(y) \equiv \theta\left(\frac{W_j}{2} - \left|y \mp \frac{L}{2}\right|\right), \quad (5)$$

$$\theta_S(y) \equiv \theta\left(\frac{W_S}{2} - |y|\right). \quad (6)$$

Here the δ function and the step function are applied to confine the physical quantities in the corresponding regions.

The SDIB parameters Z_σ can be decomposed as

$$Z_\sigma = Z_0 \pm Z_s, \quad (7)$$

where the spin-independent component Z_0 represents effects of an oxide layer or the local disorder at the interface,[1] while the spin-dependent one Z_s can be induced by ferromagnetism. The sign depends on whether a particular spin component σ is the majority (+) or minority (−) carrier. As one of the prevalent causes for an SDIB, we propose a semiclassical picture to derive Z_s as a function of the average deviation of exchange energy compared with a no-barrier case, $\langle\delta\epsilon^{\rm ex}\rangle$, over a microscopic length, ξ, associated with the interfacial properties:

$$Z_s = \tan\left(\frac{\langle\delta\epsilon^{\rm ex}\rangle\xi}{\hbar v_F}\right). \quad (8)$$

This form can be derived by considering the phase accumulation of an electron in a microscopic model passing through a finite layer having spin-dependent potentials and relating it to the phase shift in an effective model described by the BTK δ function barrier[45] (see Appendix A). Equations (7) and (8) show that for a purely magnetic interface ($Z_0 = 0$) one has

$Z_\downarrow = -Z_\uparrow$ with the magnitude sensitive to the microscopic configuration.

Now we turn to six different scattering processes through the interface, which describe the transport physics in the system. As illustrated in Fig. 1, given an electron of energy lower than the superconducting gap injected from F1, there are two local scattering processes at the F1-S interface, (1) the direct backscattering, or local normal reflection (LNR), and (2) local Andreev reflection (LAR), as well as two crossed scattering processes mediated by the superconducting order at the F2-S interface, (3) electron backscattering called elastic cotunneling, and (4) crossed Andreev reflection (CAR). For convenience in comparison, we refer to the elastic cotunneling as crossed normal reflection (CNR) in what follows. If the energy is higher than the superconducting gap, we have two more processes: (5) quasiparticle transmissions (QPT) and (6) quasihole transmissions (QHT) into the S region. In Sec. III we apply the BTK treatment to compute scattering amplitudes subject to the incoming state as well as the SDIB and hence obtain a net charge current carried by these scattering processes.

III. BTK TREATMENT

The BTK treatment is to consider charge transport as a net effect of reflections and transmissions of electrons or holes at the N-S (F-S) interface. The scattering amplitudes of reflections and transmissions are obtained by solving the BdG equation with the interface potential. In the presence of voltage drop across the interface, an induced current is computed by summing the probability current contributed by each scattering process, weighted by the Fermi distribution. The calculations are aimed at a current-voltage relation as a function of physical variables of interests, such as the interface parameters, exchange energy, geometry of the system, and temperature.

We start with the Hamiltonian of Eq. (1) for considering incoming and outgoing waves incorporating the six scattering processes (discussed in Sec. II). As prescribed by the BTK treatment, we solve for the forms of the incoming and outgoing waves by boundary condition matching. Our theoretical setup requires careful accounting of the spin species, the multiple channels, and the SDIB; we thus provide a detailed outline of the procedure below.

We consider an incoming wave of energy E from the F side ($x < 0$). The wave function is of the form of a plane wave in the $\hat{\mathbf{x}}$ direction multiplied by a bound wave in the $\hat{\mathbf{y}}$ direction. We use indexes τ,σ indicating a particle ($\tau = +$) with spin σ or a hole ($\tau = -$) with spin $\bar{\sigma}$, the channel number n labeling the bound states in the $\hat{\mathbf{y}}$ direction, and an index j denoting the wave in Fj ($j = 1,2$) regions (see Fig. 1). The incoming wave is written as

$$\Psi^{\rm in}_{\tau\sigma jn} = \left[\begin{pmatrix}\delta_{\tau+}\\0\end{pmatrix} e^{ixp^{+,j}_{\sigma,n}} + \begin{pmatrix}0\\\delta_{\tau-}\end{pmatrix} e^{-ixp^{-,j}_{\bar{\sigma},n}}\right]\Phi^j_n(y), \tag{9}$$

where δ is the δ function. The wave vectors p and the y-component wave function Φ are given below in Eqs. (12) and (14), respectively. The sign in front of of the wave vector is chosen to match the direction of the group velocity.

The outgoing wave is represented as a linear combination of degenerate scattering modes with energies and group velocities corresponding to the incoming wave. The wave functions $\Psi_{j/\rm S}(\mathbf{r})$ in Fj/S regions are separately given as

$$\Psi^{\rm out}_j = \sum_{l=1}^{M^j_a} a^j_l \begin{pmatrix}0\\1\end{pmatrix} e^{ixp^{-,j}_{\bar{\sigma},l}}\Phi^j_l(y) + \sum_{l=1}^{M^j_b} b^j_l \begin{pmatrix}1\\0\end{pmatrix} e^{-ixp^{+,j}_{\sigma,l}}\Phi^j_l(y), \tag{10}$$

$$\Psi^{\rm out}_{\rm S} = \sum_{l=1}^{M_{\rm S}} \left[c_l \begin{pmatrix}u\\v\end{pmatrix} e^{ixk^+_l} + d_l \begin{pmatrix}v\\u\end{pmatrix} e^{-ixk^-_l}\right]\Phi^{\rm S}_l(y). \tag{11}$$

Here a^j_l are the amplitudes for LAR (CAR) of channel l if j is the same as (different from) the incoming wave, and similarly b^j_l represent the LNR (CNR) processes. The amplitudes c_l (d_l) correspond to quasiparticle (quasihole) transmissions in channel l. These amplitudes of the outgoing waves are also functions of the indices $\{\tau,\sigma,j,n\}$ of the incoming wave, which have been dropped here for convenience. The quasiparticle basis u and v satisfies $u^2 = 1 - v^2 = \frac{1}{2}(1 + \sqrt{1 - \Delta^2/E^2})$. The wave vectors of the x component of the wave functions in channel l are given by

$$p^{\tau,j}_{\sigma,l} = \sqrt{1 + \tau E + \sigma\epsilon^{\rm ex}_j - (l\pi/W_j)^2}, \tag{12}$$

$$k^\tau_l = \sqrt{1 + \tau\sqrt{E^2 - \Delta^2} - (l\pi/W_{\rm S})^2}. \tag{13}$$

From here on, we take the Fermi energy and inverse of the Fermi wave vector as energy and length units ($\epsilon_{\rm F} = k^{-1}_{\rm F} = 1$), respectively. In Eq. (10), the upper bounds of the summations, $M^j_{a/b}$, are given by the highest current-carrying mode, above which a mode has a purely imaginary wave vector and hence carries no current. In Eq. (11), the wave vector can never be purely imaginary if $E < \Delta$. In such case, we choose $M_{\rm S}$ large enough to guarantee the convergence in numerical calculations.[39] The y components of the wave functions in Eqs. (12) and (13) are given by

$$\Phi^j_l = \sqrt{\frac{2}{W_j}}\sin\left[l\pi\left(\frac{y \mp L/2}{W_j} + \frac{1}{2}\right)\right]\theta_j(y), \tag{14}$$

$$\Phi^{\rm S}_l = \sqrt{\frac{2}{W_S}}\sin\left[l\pi\left(\frac{y}{W_S} + \frac{1}{2}\right)\right]\theta_S(y). \tag{15}$$

To solve for the amplitudes, we match the incoming and outgoing waves by imposing the boundary conditions at the interface ($x = 0$):

$$\Psi^{\rm in}_{\tau\sigma jn}(0,y) + \sum_{i=1}^{2}\Psi^{\rm out}_i(0,y) = \Psi^{\rm out}_{\rm S}(0,y), \tag{16}$$

$$\left[\partial_x + \begin{pmatrix}Z_{j\sigma} & 0\\0 & Z_{j\bar{\sigma}}\end{pmatrix}\right]\Psi^{\rm in}_{\tau\sigma nj}(0,y) + \sum_{i=1}^{2}\left[\partial_x + \begin{pmatrix}Z_{i\sigma} & 0\\0 & Z_{i\bar{\sigma}}\end{pmatrix}\right]\Psi^{\rm out}_j(0,y) = \partial_x\Psi^{\rm out}_{\rm S}(0,y). \tag{17}$$

Here Eq. (16) is the continuity equation, while Eq. (17) is obtained from integrating the BdG equation through the interface ($\int_{0^-}^{0^+} dx$). For $Z_{i\sigma} = Z_{i\bar{\sigma}}$, Eq. (17) reduces to the boundary condition for the case of a spin-independent interface discussed in Ref. 39. We substitute the wave functions in Eqs. (9)–(11) into Eq. (16) and project it onto channel m in the S region,

$$\begin{pmatrix}\delta_{\tau+}\\ \delta_{\tau-}\end{pmatrix}\Lambda^j_{nm} + \sum_{i=1}^{2}\left[\begin{pmatrix}0\\1\end{pmatrix}\sum_{l=1}^{M_a^i}\Lambda^i_{lm}a^i_l + \begin{pmatrix}1\\0\end{pmatrix}\sum_{l=1}^{M_b^i}\Lambda^i_{lm}b^i_l\right] = \begin{pmatrix}u\\v\end{pmatrix}c_m + \begin{pmatrix}v\\u\end{pmatrix}d_m, \tag{18}$$

where

$$\Lambda^j_{lm} = \int dy\,\Phi^j_l(y)\Phi^{\mathrm{S}}_m(y). \tag{19}$$

Similarly, we substitute the wave functions into Eq. (17) and project it onto the channel m in the Fi region,

$$\begin{aligned}&\begin{pmatrix}p^{+,j}_{\sigma,n} - iZ_{j\sigma} & 0\\ 0 & -p^{-,j}_{\bar{\sigma},n} - iZ_{j\bar{\sigma}}\end{pmatrix}\begin{pmatrix}\delta_{\tau+}\\ \delta_{\tau-}\end{pmatrix}\delta_{ij}\delta_{mn}\\ &+\begin{pmatrix}-p^{+,i}_{\sigma,m} - iZ_{i\sigma} & 0\\ 0 & p^{-,i}_{\bar{\sigma},m} - iZ_{i\bar{\sigma}}\end{pmatrix}\\ &\times\left[\begin{pmatrix}0\\1\end{pmatrix}a^i_m + \begin{pmatrix}1\\0\end{pmatrix}b^i_m\right]\\ &= \sum_{l=1}^{M_{\mathrm{S}}}\Lambda^i_{ml}\left[k^+_l\begin{pmatrix}u\\v\end{pmatrix}c_l - k^-_l\begin{pmatrix}v\\u\end{pmatrix}d_l\right].\end{aligned} \tag{20}$$

Using Eq. (18) to replace c_l and d_l in Eq. (20), we rewrite the right-hand side of Eq. (20) as

$$\Omega^{ij}_{mn}\begin{pmatrix}\delta_{\tau+}\\ \delta_{\tau-}\end{pmatrix} + \sum_{k=1}^{2}\left[\sum_{l=1}^{M_a^k}\Omega^{ik}_{ml}\begin{pmatrix}0\\1\end{pmatrix}a^k_l + \sum_{l=1}^{M_b^k}\Omega^{ik}_{ml}\begin{pmatrix}1\\0\end{pmatrix}b^k_l\right], \tag{21}$$

where Ω^{ij}_{mn} is a 2×2 matrix defined as

$$\Omega^{ij}_{mn} \equiv \begin{pmatrix}u & v\\ v & u\end{pmatrix}\left[\sum_{l=1}^{M_{\mathrm{S}}}\Lambda^i_{ml}\Lambda^j_{nl}\begin{pmatrix}k^+_l & 0\\ 0 & -k^-_l\end{pmatrix}\right]\begin{pmatrix}u & v\\ v & u\end{pmatrix}^{-1}. \tag{22}$$

Combining Eqs. (20)–(22) and letting i run from 1 to 2 as well as m run through all current-carrying channels, we get a set of linear equations for obtaining the amplitudes a^i_m and b^i_m.

Next we turn to compute the probability currents, which in turn yield the current-voltage relation. The probability currents for wave functions of a Nambu form, $(\psi_1\psi_2)^{\mathrm{T}}$, are defined as

$$\mathbf{J} = \frac{\hbar}{m}\mathrm{Im}(\psi_1^*\nabla\psi_1 - \psi_2^*\nabla\psi_2), \tag{23}$$

where the ψ_1 term represents the contribution from electrons and the ψ_2 term does that of holes. The wave functions in Eqs. (9)–(11) carry no current in the $\hat{\mathbf{y}}$ direction. The outgoing probability currents in the $\hat{\mathbf{x}}$ direction at the interface ($x = 0$) in the ferromagnet and superconductor regions [$\tilde{J}(E)$ and $\tilde{J}^{\mathrm{S}}(E)$, respectively] are given by

$$\tilde{J}^{\tau'\sigma'j'n'}_{\tau\sigma jn} = \frac{\hbar}{m}\left[\delta_{\tau'-}\left|a^{j'}_{n'}\right|^2\mathrm{Re}\left(p^{-,j'}_{\sigma',n'}\right) - \delta_{\tau'+}\left|b^{j'}_{n'}\right|^2\mathrm{Re}\left(p^{+,j'}_{\sigma',n'}\right)\right]/J^{\mathrm{in}}_{\tau\sigma jn}, \tag{24}$$

$$\tilde{J}^{\mathrm{S};\tau'n'}_{\tau\sigma jn} = \frac{\hbar}{m}[\delta_{\tau'+}|c_{n'}|^2\mathrm{Re}(k^+_{n'}) + \delta_{\tau'-}|d_{n'}|^2\mathrm{Re}(k^-_{n'})] \times(|u|^2 - |v|^2)/J^{\mathrm{in}}_{\tau\sigma jn}, \tag{25}$$

normalized by the incoming current,

$$J^{\mathrm{in}}_{\tau\sigma jn} = \frac{\hbar}{m}\left(\delta_{\tau+}p^{+,j}_{\sigma,n} + \delta_{\tau-}p^{-,j}_{\bar{\sigma},n}\right). \tag{26}$$

Here the subscripts (superscripts) denote the corresponding incoming (outgoing) state. In Eq. (24), $\{\tau',\sigma'\} = \pm\{\tau,\sigma\}$ represents normal or Andreev reflections, respectively, while $j' = j$ or $\bar{j}$ (the counterpart of j) denotes local or crossed processes, respectively.

We assume the bias voltage V to be the same across both F leads and the S electrode, as set up in the experiment of Ref. 38. We remark that our method can also be applied to the case of different voltages on different leads. Such a scenario could enable one to probe other physical properties, such as current correlation[46] and long-range entanglement, in the system.

Following the standard BTK formalism,[1,39] we obtain the charge current I carried by incoming particles or holes ($\tau = \pm$) with σ spin in channel n in lead Fj (Appendix B),

$$\begin{aligned}&I_{\tau\sigma jn}(V)\\ &= \tau e\int_0^\infty dE\left\{\left(1 - \sum_{j'}\sum_{n'}\left|\tilde{J}^{\tau\sigma j'n'}_{\tau\sigma jn}\right|\right)[f_0(E - \tau eV)\right.\\ &\left. - f_0(E)] + \sum_{j'}\sum_{n'}\left|\tilde{J}^{\bar{\tau}\bar{\sigma}j'n'}_{\tau\sigma jn}\right|[f_0(E) - f_0(E + \tau eV)]\right\},\end{aligned} \tag{27}$$

up to a constant associated with density of states, Fermi velocity, and an effective cross-sectional area.[39] Here $f_0(E) = [\exp(E/k_BT) + 1]^{-1}$ is the Fermi distribution function at temperature T, and $\bar{\tau} = -\tau$. The total charge current is obtained by summing over all contributions from the incoming waves,

$$I(V) = \sum_{\tau=\pm}\sum_{\sigma=\pm}\sum_{j=1,2}\sum_{n} I_{\tau\sigma jn}. \tag{28}$$

Notice that I is also a function of Δ, ϵ_{ex}, T, $Z_{j\sigma}$, and the geometry of the system (characterized by L and $W_{1/2/\mathrm{S}}$ here). Equipped with this form for the current across the interface, we are now in a position to explore it under various conditions.

IV. RESULTS

In this section we present major differences in transport properties resulting from SDIB, compared to the previous BTK studies.[39] The key physical quantity showing such differences is the normalized relative resistance δR, defined as resistance difference between two cases of the device that have parallel (P) or antiparallel (AP) magnetization alignment of the two F

leads,

$$\delta R = \frac{R_{\rm AP} - R_{\rm P}}{(R_{\rm AP} + R_{\rm P})/2} = \frac{I_{\rm P} - I_{\rm AP}}{(I_{\rm P} + I_{\rm AP})/2}, \tag{29}$$

where $I_{\rm P(AP)}$ is the total current obtained from Eq. (28) for the corresponding cases and $R_{\rm P(AP)} = V/I_{\rm P(AP)}$. The P (AP) case is characterized by the same (opposite) signs of the exchange energies in the two F leads, which leads to their majority spin species being the same (opposite). Previous calculations in Ref. 39 show that δR is always nonpositive, no matter how the barrier strength, exchange energy, geometry of the device, and temperature vary. This result is as expected of singlet-paired superconductors and in and of itself would indicate that the AP case always carries more current than the P case given the same bias voltage, in conflict with the experimental results in Ref. 38. Here we show the exact manner in which the SDIB would alter this expected trend.

In the following calculations, we take the majority spin in F1 to be $\uparrow$, $\epsilon_2^{\rm ex} = \pm\epsilon_1^{\rm ex}$ for the P (AP) case, and $eV = 10^{-2}\Delta(\text{at } 0T) = 2 \times 10^{-5}\epsilon_F$ (corresponding to a Pippard superconducting coherence length[47,48] $\sim 500k_F^{-1}$ in our case), all of which are typical values in experiments. We first consider zero temperature where the system is in the subgap regime and no quasiparticle transmission occurs. We analyze the effect of two factors, ferromagnetism as well as geometry, on which δR shows strong dependence and discuss how SDIB are relevant to the results. Then we study the finite-temperature case where Δ varies in temperature and quasiparticle transmission contributes to the conductivity.

A. Effects of ferromagnetism

The effects of ferromagnetism on the charge transport emerge in two ways. The first is that the presence of $\epsilon^{\rm ex}$ in the F leads results in a density imbalance in spin species and thus alters both the number of channels and the momentum of particles [see Eq. (12)] responsible for carrying charge current. The second is that $\epsilon^{\rm ex}$ in the interface region constitutes SDIB parameters Z (as discussed in Sec. II), which lead to different scattering phases between majority and minority spins, and in turn to interference in the scattering wave function, as we will see in subsequent discussions and results.

Mathematically, this can be seen by noting in Eq. (24) that the current is a product of particle momentum p associated with the first effect, and scattering magnitudes $|a|$ and $|b|$ altered mainly by the second effect. The number of channels $M_{a/b}^j$ (discussed in Sec. III) also reflects the imbalance effect and plays a role when we add up the probability current in Eqs. (27) and (28). Both effects contribute to a difference in behavior between the P and AP cases solely due to the presence of coherent crossed transport (CNR and CAR). This can be seen by noting that in the absence of these processes, for instance, for large separation between F leads, each lead can be treated independently and thus the P and AP cases would show the same results. On the other hand, the CNR and CAR processes distinguish the fact that in the P case the majority spin species are the same in both leads but are different in the AP case. We expect that the first effect is obscured in the low imbalance regime where the majority and minority species are less distinguishable, while the second effect is suppressed when the interface barrier is nearly spin independent ($Z_s \sim 0$).

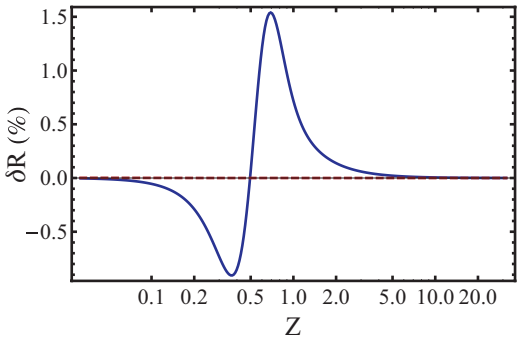

FIG. 2. (Color online) Relative resistance δR (defined as $(R_{\rm AP} - R_{\rm P})/[(R_{\rm AP} + R_{\rm P})/2]$) vs interface parameters Z. The solid curve is for a purely spin-dependent barrier ($Z_0 = 0$, $Z_s = Z$) while the dashed curve is for a spin-independent one ($Z_0 = Z$, $Z_s = 0$). Data presented are for the system parameters $W_1 = W_2 = L = 10k_F^{-1}$, $W_S = 100k_F^{-1}$, $\epsilon^{\rm ex} = 0.01\epsilon_F$, $\Delta = 0.002\epsilon_F$, and $T = 0$.

In this subsection we choose the set of parameters $W_1 = W_2 = L = 10k_F^{-1}$, $W_S = 100k_F^{-1}$, and zero temperature ($T = 0$). Figure 2 shows δR as a function of a purely SDIB ($Z_0 = 0$ and Z_s varied, solid curve) and a spin-independent case ($Z_s = 0$ and Z_0 varied, dashed curve) at a small imbalance of $\epsilon^{\rm ex} = 0.01\epsilon_F$. We see that a purely SDIB causes an obvious variance of δR in both positive and negative values at an intermediate Z_s. At large Z_s the barrier is high enough such that most incidence is directly reflected while at small Z_s the phase shift between majority and minority spins is close to zero, both of which make the difference between P and AP cases negligible and hence give $\delta R \sim 0$. For the spin-independent barrier, there is almost no difference between P and AP, so δR is always flat and close to zero (still negative, reflecting the small imbalance effect as discussed before). A complete dependence of δR on both Z_0 and Z_s is shown in the contour plot in Fig. 3. We see that δR is negative for most of the parameter space and only becomes positive when Z_s dominates.

Although the maximum magnitude in the positive region is one order smaller than that in the negative one, there is a wide enough parameter regime for $0.1\% < \delta R < 1.5\%$, the same order magnitude observed in the experiment of Ref. 38. The most negative value is centered around the region of line $Z_0 = Z_s$ where either majority or minority spins are subject to an almost transparent interface. This is because in the AP case different spin species in the two F leads see the transparent barrier, so the CAR is greatly enhanced and hence reduces the resistance compared to the P case. Notice that there is a small positive region at $Z_s < Z_0$ with $0 < \delta R < 10^{-4}$. However, for $Z_s = 0$, δR is always negative, indicating that the SDIB is essential for positive δR. The contour plot of Fig. 3 remains unchanged if $Z_s \to -Z_s$.

We now analyze the effect of density imbalance. Figure 4 shows comparison of δR as a function of $\epsilon^{\rm ex}$ for two purely SDIB conditions where δR is initially positive ($Z_s = 0.7$, solid curve) and negative ($Z_s = 0.4$, dashed) at zero exchange, as well as for a spin-independent condition ($Z_0 = 0.7$, dotted). First we see that at large imbalance all curves drop to the highly negative region. This is due to a combination of

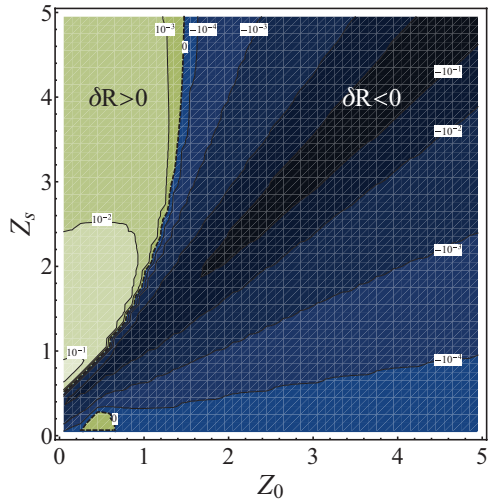

FIG. 3. (Color online) Contour plot of δR in the plane of Z_0 and Z_s. The positive (lighter green) and negative (darker blue) regions are separated by a dashed contour indicating $\delta R = 0$. A weakly positive δR region appears close to the line of $Z_s = 0$, for which δR is always negative.

number of channels and the momentum for the minor species monotonically decreasing with the increase in ϵ^{ex}, as shown in Eq. (12). This decrease reduces current carried by all Andreev processes involving one majority and one minority spin; CAR in AP case is not reduced as it involves two majority spins in the two F leads. At large imbalance in the P case most incoming current directly reflects and leaves small net current compared to AP case. Therefore δR drops and finally reaches its maximum value of -2 [see Eq. (29)] at which $I_P = 0$ (see inset).

The imbalance has a monotonic influence on the transport, explaining the curve for the case of spin-independent barrier. For an SDIB, however, δR exhibits an overall decreasing trend but a locally (e.g., in $0.5 < \epsilon^{ex}/\epsilon_F < 0.7$) nonmonotonic form as a function of ϵ^{ex}. We attribute this behavior to an interference effect of scattering through the SDIB. Differing interference effects between the P and AP cases can thus either enhance or compete with the imbalance effect and dominate over it to make δR largely negative or even positive at low imbalance.

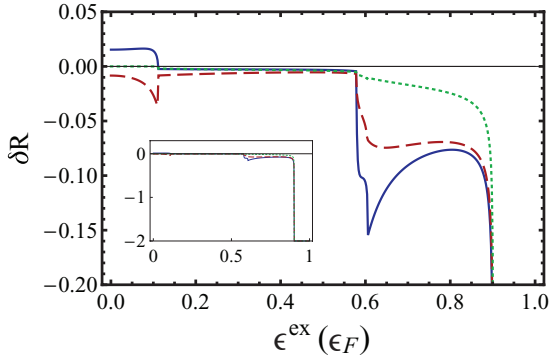

FIG. 4. (Color online) Relative resistance δR vs exchange energy ϵ^{ex} at the interface parameters $\{Z_0, Z_s\} = \{0,0.7\}$ (solid curve), $\{0,0.4\}$ (dashed), and $\{0.7,0\}$ (dotted). Inset: A zoom-out that shows δR dropping to -2 at large imbalance.

We further investigate the imbalance effect by looking at four different contributions to the total current: the currents carried by (1) the incoming electrons and LNR, (2) CNR, (3) LAR, and (4) CAR [I^{LN}, I^{CN}, I^{LA}, and I^{CA}, respectively, defined in Eq. (B5) in Appendix B]. Figure 5 shows these components and their combined effect as a function of ϵ^{ex} for P (top row) and AP (middle row) cases as well as the difference between P and AP (bottom row) at various interface conditions (corresponding to different columns). We first see that the SDIB cases have more current (lower resistance) than the spin-independent cases of the same barrier strength. For all cases the two local currents are the dominant contributions to the total current and are comparable in magnitude. Their monotonically decreasing trends are consistent with an increase in imbalance, except I^{LN} in the low-imbalance regime ($\epsilon^{ex} < 0.11\epsilon_F$) in the case of a purely SDIB of $Z_s = 0.4$ (the rightmost column), which reflects a stronger interference effect than the imbalance effect. The two crossed currents have such small contributions compared to the local current that they are almost indiscernible from zero in the figure, except I^{CA} in the high-imbalance regime in the two SDIB cases, which indicates a great enhancement in long-range entanglement. The difference in current between P and AP cases, $\delta I = I_P - I_{AP}$ [directly related to δR via Eq. (29)], is one to two orders smaller than either I_P or I_{AP} and is highly sensitive to the value of the exchange field.

The two spin-independent cases have a similar behavior: At low imbalance the compensation of dominant contributions of δI^{LN} and δI^{CN} makes the total δI close to zero (still negative), while at high imbalance δI^{CA} has a large negative contribution and δI^{LA} is suppressed, as supported by the imbalance effect.

The purely SDIB cases have various dominant contributions at low imbalance. At $Z_s = 0.7$ (the second column from left), the dominant contribution is positive δI^{LN}, making the sum of the contributions positive, while at $Z_s = 0.4$ (the rightmost column) the strong negative δI^{CN} makes the sum negative. These results can only be attributed to the interference of scattering through an SDIB. At high imbalance, δI^{CA} dominates as in the spin-independent case but is much larger, due to the greater enhancement of I^{CA} in the AP case. Notice that all the curves have kinks at the same positions—this is due to the reduction in the number of scattering channels by one at each kink.

In brief, we analyzed the effects of spin imbalance and scattering through an SDIB, both induced by ferromagnetism. The former monotonically lowers δR toward negative values and dominates in the high-imbalance regime, while the latter exhibits its influence in positive or negative directions, where the trend is revealed in the scattering magnitudes. A system with an SDIB can sustain a significant large CAR current in the AP case, reminiscent of a great enhancement of long-range entanglement.

B. Effects of geometry

The signature of interference due to scattering between the two F leads implies a strong dependence of the transport properties on their geometry. We examine δR as a function of the widths, W_1 and W_2, and the separation, L, of the leads at a low imbalance value of $\epsilon^{ex} = 0.01\epsilon_F$ where the scattering

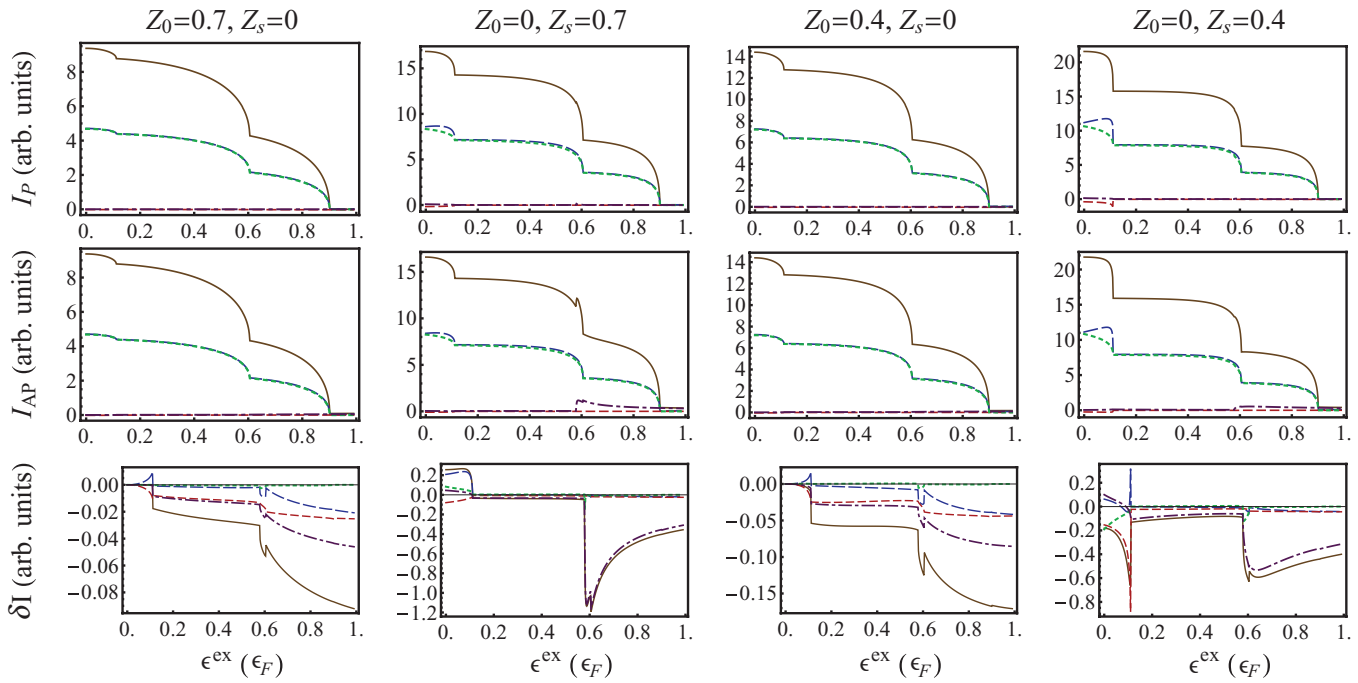

FIG. 5. (Color online) Local normal, local Andreev, crossed normal, cross Andreev currents, and their combined effect (blue long-dashed, green dotted, red short-dashed, purple dot-dashed, and brown solid curves, respectively) vs exchange energy ϵ^{ex}. From top to bottom rows presents the current of the P case, I_P, AP case, I_{AP}, and the difference, $\delta I = I_P - I_{AP}$, respectively. The first and second columns correspond to a spin-independent barrier and a purely SDIB of strength 0.7, respectively, while the third and fourth correspond to strength 0.4. Remarkably, the dot-dashed curves (contributed by CAR) at $\epsilon^{ex} > 0.6\epsilon_F$ in panels of the bottom row show much larger values for SDIB (nonzero Z_s) than those for the spin-independent barrier ($Z_s = 0$), indicating a strong enhancement of CAR in the P case. The coincidence of two curves in some regions indicates the two local (crossed) currents almost equal to each other.

effects dominate. Here we fix $W_S = 100k_F^{-1}$. Figure 6 shows δR vs L at three barrier conditions, $\{Z_0, Z_s\} = \{0,0.7\}, \{0,0.4\}$, and $\{0.7,0\}$, as presented in Fig. 4. For the two SDIB cases, the curves modulate and exponentially decay to zero at large L. The oscillation period is π (in units of k_F^{-1}), which results from a 2π modulation in the scattering amplitudes, which in turn owe to the oscillatory behavior of matrix Ω in Eq. (22). Since the quantity Λ in Eq. (19) is a sinusoidal function in $W_{1/2/S}$ and L, summing the product of Λ in calculating Ω

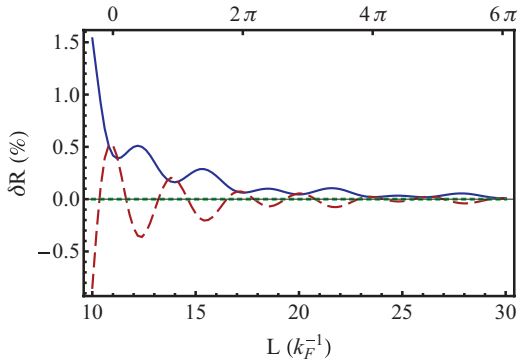

FIG. 6. (Color online) Relative resistance, δR, vs the separation between two F leads, L, with fixed $W_{1(2)}$ ($W_1 = W_2 = 10k_F^{-1}$) at the interface parameters $\{Z_0, Z_s\} = \{0,0.7\}$ (solid curve), $\{0,0.4\}$ (dashed), and $\{0.7,0\}$ (dotted), same as presented in Fig. 4. Relative distance from a reference is marked on top of graph, showing the oscillatory period of π.

directly indicates a relation between the interference and the geometry of the system. At large L, the scattering hardly shows a difference between P and AP cases. The fast decay as a function of L is governed by a power-law factor in L/k_F^{-1} due to the interference rather than an exponential factor associated with the Pippard coherence length ($\sim 500k_F^{-1}$) (discussed in Ref. 39). For the spin-independent barrier, the curve is flat and close to zero as expected. Notice that the modulations in the current for P and AP cases still exist (as discussed in Ref. 39). However, they modulate in-phase and cancel out in the form of δR.

Figure 7 shows contour plots of δR in the plane of W_1 and W_2 at $L = (W_1 + W_2)/2$ for the pure SDIB cases of $Z_s = 0.7$ [panel (a)] and 0.4 [panel (b)]. We see δR modulates with a period of π in both W_1 and W_2 directions, for the same reason as for variation in L. In (a), δR is always positive and becomes close to zero at large W_1 and W_2. In (b), the value is mainly positive with a slower decay as W_1 and W_2 go large. Both plots show a wide parameter range for positive δR in contrast to the small negative value expected in the case of spin-independent barriers.

Finally we keep relative ratios between W_1, W_2, W_S, and L unchanged and enlarge the whole device (making it closer to some of the realistic systems[38]). Figure 8 shows δR as a function of a pure SDIB parameter Z_s for three difference scales of the device: the one of $W_1 = W_2 = L = 10k_F^{-1}$ and $W_S = 100k_F^{-1}$ (solid curve, same as presented in Fig. 2) as well as 10 and 30 times the case of the solid curve (dashed and dotted curves, respectively). When the system becomes an order of

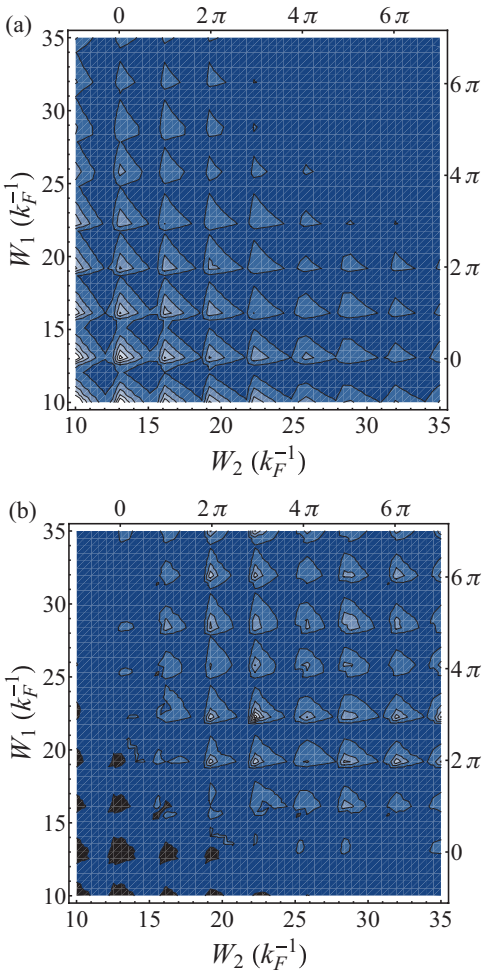

FIG. 7. (Color online) Contour plot of δR in the plane of W_1 and W_2. Data presented for a pure SDIB of $Z_s = 0.7$ (a) and 0.4 (b). The lowest contour is zero, below which the value is negative (corresponding to the black region). The magnitude difference between the contours is 0.2%. Relative distance from a reference is marked on top and right of graph, showing the oscillatory period of π.

magnitude larger, the positive δR region expands but its value is more than one order smaller. Because larger sizes result in more conducting channels and hence more interference among them, this trend can smear out the difference between P and AP cases and leave a small δR. To improve the modeling for a real system that can still have δR of a few percent, new ingredients such as the dependence of Z parameters on spatial coordinate or on channels would be needed.

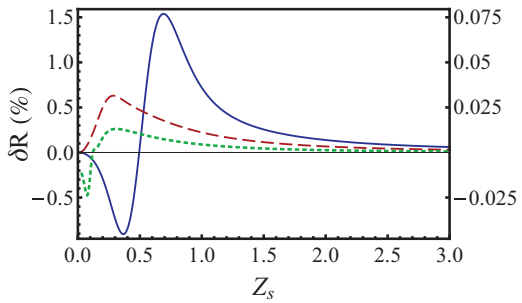

FIG. 8. (Color online) Relative resistance δR vs pure SDIB Z_s. The solid curve (axis on the left of the graph) presents a purely SDIB system of $W_1 = W_2 = L = 10k_F^{-1}$ and $W_S = 100k_F^{-1}$ (same as presented in Fig. 2). The dashed and dotted curves (axis on the right of the graph) are for devices with sizes 10 and 30 times that for the solid curve, respectively.

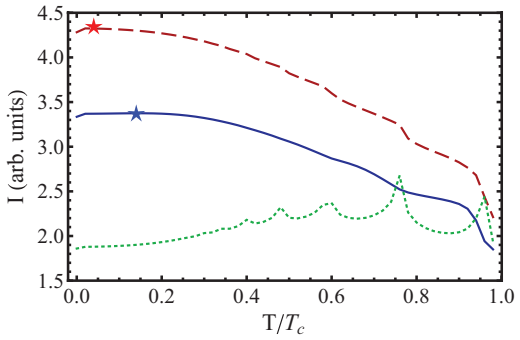

FIG. 9. (Color online) Charge current I vs the temperature T for the P case at the interface parameters $\{Z_0, Z_s\} = \{0,0.7\}$ (solid curve), $\{0,0.4\}$ (dashed), and $\{0.7,0\}$ (dotted), as presented in Fig. 4. The star signs indicate position of the maximum point of the corresponding curves.

C. Effects of temperature

Finally, we briefly study finite-temperature effects. Here, two factors need to be incorporated: (1) quasiparticle (hole) transmissions (QPT and QHT, respectively) that arise from thermal fluctuations and participate in charge transport as well as (2) the decrease in the superconducting gap as a function of temperature, $\Delta(T) = \Delta(0)\sqrt{1 - T/T_c}$. Here, we focus on the effect of the SDIB and thus choose the case of low polarization for which the effects of SDIB are most prominent. We plot the current in the P case, I_{AP}, vs temperature, T, for different barrier conditions in Fig. 9. All cases show suppressed conductance for a significant temperature regime close to T_c due to the vanishing superconductivity. The spin-independent interface shows local peaks which we attribute to thermal population of new channels. Spin dependence of the barrier suppresses these peaks. We also mention that in accordance with BTK expectations,[1] while the SDIB curves seem to decrease as a function of temperatures, the maximum (star

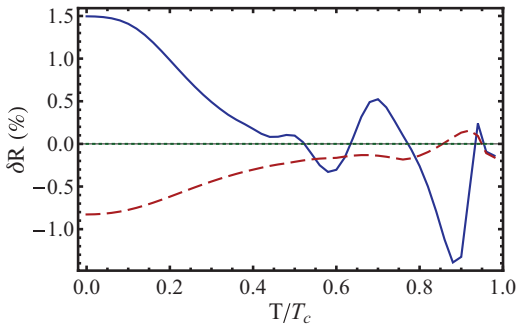

FIG. 10. (Color online) Relative resistance δR vs the temperature T at the interface parameters $\{Z_0, Z_s\} = \{0,0.7\}$ (solid curve), $\{0,0.4\}$ (dashed), and $\{0.7,0\}$ (dotted), convention as presented in Fig. 9. Notice that the dotted curve almost coincide with the axis.

signs in graph) occurs at nonzero but very low temperature, indicating a reentrant effect.

To characterize the difference between P and AP cases, we plot δR vs T for the same set of parameters in Fig. 10. We see that δR can be smooth, widely fluctuating, or even endowed with a sign change for different SDIB conditions. The salient feature here is that in the spin-independent case, due to the low polarization, δR is exceedingly small and constant on the scale shown. However the SDIB cases show that temperature can alter the sign of δR and what might have started as negative at low temperature can reverse the trend. The lack of trend has also been found in different samples in experiment.[38]

V. CONCLUSION

In this paper, we studied electronic transport physics in superconductor–double ferromagnet (S-FF) junctions with spin-dependent interface barriers (SDIB) using the Blonder-Tinkham-Klapwijk (BTK) treatment. We proposed spin-dependent Z parameters modeling SDIB for the BTK calculations and discussed its relation to microscopic physical quantities at the interface. Our extended model is one of the first incorporating SDIB for S-FF junctions and shows that SDIB can increase crossed Andreev reflection (CAR) current. We found that SDIB can cause interference in wave functions of CAR and other scattering processes that can either collaborate or compete with the imbalance effect in the F leads. This competition can cause more current carried by F leads of parallel (P) magnetization than by the antiparallel (AP) case (resulting in a positive δR), which does not occur in the case of spin-independent barriers. Our calculations showed that positive δR is stable in a sufficiently large parameter regime as a function of Z parameters, magnetization, geometry of the system, and temperature. At low magnetization, the effects of SDIB are responsible for the different transport between P and AP cases, resulting in positive or negative δR that is sensitive to the Z parameters. At high magnetization, δR is always negative due to the population imbalance in the F leads, and SDIB contributes large additional enhancement of CAR in the AP case. Variance in the geometry of the junction results in oscillations in δR, which reveal the interference effects on the transport physics.

Our studies suitably describe recent experiments of Ref. 38 and can be used as a guide for further investigation in such settings, including the possibility of controlled tuning of S-F interface properties in the presence of artificially grown SDIB barriers. Our model easily extends to a wide class of multiterminal hybrid junctions. An important ingredient to take into account in the future, particularly to explain differing P versus AP behavior, is to incorporate induced spin-triplet correlations together with the spin-flip scatterers.[18,49–53] This would be particularly relevant to currently intense explorations of coherent properties and long-range entanglement in superconductor heterostructures.

ACKNOWLEDGMENTS

This work is supported by the DARPA-ARO Award No. W911NF-07-1-0464 (K.S.), by the University of Cincinnati (N.S.), and by NSF Grant No. DMR-0906521 (S.V.). N.S. and S.V. acknowledge the hospitality of the Aspen Center for Physics. We are grateful to Madalina Colci and Dale J. Van Harlingen for motivating these studies and for valuable input.

APPENDIX A: SEMICLASSICAL PICTURE FOR SDIB

In this section we use a semiclassical picture to model the spin-dependent component of the SDIB parameter, Z_s, in Eq. (7). In the original BTK treatment,[1] Z is considered as a phenomenological barrier parameter capable of characterizing distinct properties of the interface, such as a metallic or insulating one. In our extended model for the SDIB, the Z parameters ought to reflect general concepts in the spin-related transport, such as the spin-dependent interfacial phase shift.[19] Based on this assumption, we derive Z_s by relating the phase shifts between scattering through the phenomenological δ-function barrier and that through the microscopic Zeeman potential at the interface, provided the spin-independent component $Z = 0$. Microscopically, an injected spin passes through the barrier region and accumulates a phase shift ϕ in the interface region, compared with the case without a barrier. In a semiclassical picture, the phase shift due to the deviation of the exchange energy (compared with the no-barrier case), $\delta\epsilon^{\rm ex}(x)$, is

$$\phi = \int_0^{t_0} \frac{\delta\epsilon^{\rm ex}(x(t))}{\hbar} dt = \int_0^{\xi} \frac{\delta\epsilon^{\rm ex}(x)}{\hbar v_F} dx \equiv \frac{\xi \langle \delta\epsilon^{\rm ex} \rangle}{\hbar v_F}, \quad \text{(A1)}$$

where t_0 is the total time to pass the barrier, v_F is the Fermi velocity, $\delta\epsilon^{\rm ex}(x(t))$ is the local deviation of exchange energy when the particle passes the position x at time t, and $\langle \delta\epsilon^{\rm ex} \rangle$ is its average over the width of the interface, ξ. Here $x = v_F t$ given that the energy variance is small compared to the Fermi energy.

Now we compare the phase shifts with those of a scattering problem having the δ-function potential,

$$-\frac{\hbar^2}{2m}\partial_x^2 + \hbar v_F Z_s \delta(x). \quad \text{(A2)}$$

By solving the Schrödinger equation for an incoming wave around the Fermi surface, we obtain Z_s as a function of the phase shift of the transmitted wave,

$$Z_s = -\tan\phi. \quad \text{(A3)}$$

Substituting Eq. (A3) into Eq. (A1), we derive the aimed relation of Eq. (8). The tangent function implies that Z_s in nonmonotonic in and sensitive to the exchange energy and microscopic length. Notice that the majority and minority spins have opposite exchange energy which leads to different signs for the spin-dependent Z parameter. In this paper we choose $\pm Z_s$ for majority (minority) spins, as shown in Eq. (7). Notice that our focus here is one of the scattering-related causes for an SDIB. We perceive that other effective treatments, such as first-principles methods,[54–56] can be applied for further analysis.

APPENDIX B: I-V RELATION

In this section we detail the calculations for current-voltage relations in the SFF junction following the standard BTK formalism[1,39] and identify the current contributions for

each scattering process. The total current contributed by an incoming wave characterized by indices $\{\tau\sigma jn\}$ is given by

$$I_{\tau\sigma jn} = A\tau \int_0^\infty dE[f_{\rightarrow}(E) - f_{\leftarrow}(E)], \tag{B1}$$

where A is a constant associated with density of states, Fermi velocity, and an effective cross-sectional area and $f_{\rightarrow(\leftarrow)}$ denotes the incoming (outgoing) populations

$$f_{\rightarrow}(E) = f_0(E - \tau eV), \tag{B2}$$

$$f_{\leftarrow}(E) = \sum_{\{\tau',\sigma'\}=\pm\{\tau,\sigma\}} \sum_{j'} \sum_{n'} \left|\tilde{J}^{\tau'\sigma' j' n'}_{\tau\sigma jn}\right| f_0(E - \tau' eV) + \sum_{\tau'=\pm} \sum_{n'} \left|\tilde{J}^{\mathrm{S};\tau' n'}_{\tau\sigma jn}\right| f_0(E). \tag{B3}$$

Here we replace the distribution function for holes in the F regions as $1 - f_0(-E - eV) = f_0(E + eV)$. By substituting Eqs. (B2) and (B3) into Eq. (B1) as well as applying a conservation relation for the probability currents,

$$\sum_{\{\tau',\sigma'\}=\pm\{\tau,\sigma\}} \sum_{j'} \sum_{n'} \left|\tilde{J}^{\tau'\sigma' j' n'}_{\tau\sigma jn}\right| + \sum_{\tau'=\pm} \sum_{n'} \left|\tilde{J}^{\mathrm{S};\tau' n'}_{\tau\sigma nj}\right| = 1,$$

we eliminate the contributions from quasiparticle transmissions and hence derive the I-V relation of Eq. (27), as a function of only processes in F regions. By summing over the incoming degrees of freedom, we obtain the total current as in Eq. (28), or simplified at zero temperature as

$$I(V,T=0) = A \sum_{\sigma=\pm} \sum_{n} \sum_{j=1,2} \int_0^{eV} dE \times \left[1 + \sum_{n'} \sum_{j'=1}^{2} \left(\left|\tilde{J}^{+\bar{\sigma} n' j'}_{-\sigma nj}\right| - \left|\tilde{J}^{+\sigma n' j'}_{+\sigma nj}\right|\right)\right]. \tag{B4}$$

From Eq. (B4) we identify four components of the total current in the subgap regime below: the local normal current I^{LN} contributed by the incoming wave and LNR, as well as the crossed normal current I^{CN}, the local Andreev current I^{LA}, and the crossed Andreev current I^{CA} contributed by CNR, LAR, and CAR, respectively:

$$\begin{aligned} I^{\mathrm{LN}} &= A \sum_{\sigma=\pm} \sum_{n,n'} \sum_{j=1,2} \int_0^{eV} dE \left(1 - \left|\tilde{J}^{+\sigma n' j}_{+\sigma nj}\right|\right), \\ I^{\mathrm{CN}} &= A \sum_{\sigma=\pm} \sum_{n,n'} \sum_{j=1,2} \int_0^{eV} dE \left(-\left|\tilde{J}^{+\sigma n' \bar{j}}_{+\sigma nj}\right|\right), \\ I^{\mathrm{LA(CA)}} &= A \sum_{\sigma=\pm} \sum_{n,n'} \sum_{j=1,2} \int_0^{eV} dE \left|\tilde{J}^{+\bar{\sigma} n' j(\bar{j})}_{-\sigma nj}\right|. \end{aligned} \tag{B5}$$

[1] G. E. Blonder, M. Tinkham, and T. M. Klapwijk, Phys. Rev. B **25**, 4515 (1982).
[2] C. W. J. Beenakker, Rev. Mod. Phys. **69**, 731 (1997).
[3] C. Lambert and R. Raimondi, J. Phys.: Condens. Matter **10**, 901 (1998).
[4] M. Eschrig, Phys. Rev. B **80**, 134511 (2009).
[5] J. M. Byers and M. E. Flatté, Phys. Rev. Lett. **74**, 306 (1995).
[6] S. Takahashi, H. Imamura, and S. Maekawa, Phys. Rev. Lett. **82**, 3911 (1999).
[7] G. Deutscher and D. Feinberg, Appl. Phys. Lett. **76**, 487 (2000).
[8] P. Recher, E. V. Sukhorukov, and D. Loss, Phys. Rev. B **63**, 165314 (2001).
[9] G. Falci, D. Feinberg, and F. W. J. Hekking, Europhys. Lett. **54**, 255 (2001).
[10] R. Mélin and D. Feinberg, Eur. Phys. J. B **26**, 101 (2002).
[11] R. Mélin and S. Peysson, Phys. Rev. B **68**, 174515 (2003).
[12] Z. C. Dong, R. Shen, Z. M. Zheng, D. Y. Xing, and Z. D. Wang, Phys. Rev. B **67**, 134515 (2003).
[13] S. Russo, M. Kroug, T. M. Klapwijk, and A. F. Morpurgo, Phys. Rev. Lett. **95**, 027002 (2005).
[14] J. P. Morten, A. Brataas, and W. Belzig, Phys. Rev. B **74**, 214510 (2006).
[15] G. Metalidis, M. Eschrig, R. Grein, and G. Schön, Phys. Rev. B **82**, 180503 (2010).
[16] G. Burkard, J. Phys.: Condens. Matter **19**, 233202 (2007).
[17] A. I. Buzdin, Rev. Mod. Phys. **77**, 935 (2005).
[18] F. S. Bergeret, A. F. Volkov, and K. B. Efetov, Rev. Mod. Phys. **77**, 1321 (2005).
[19] A. Cottet and W. Belzig, Phys. Rev. B **72**, 180503(R) (2005).
[20] J. Linder, T. Yokoyama, A. Sudbo, and M. Eschrig, Phys. Rev. Lett. **102**, 107008 (2009).
[21] M. Fogelström, Phys. Rev. B **62**, 11812 (2000).
[22] Y. S. Barash and I. V. Bobkova, Phys. Rev. B **65**, 144502 (2002).
[23] J. Kopu, M. Eschrig, J. C. Cuevas, and M. Fogelstrom, Phys. Rev. B **69**, 094501 (2004).
[24] M. Fauré, A. I. Buzdin, A. A. Golubov, and M. Yu. Kupriyanov, Phys. Rev. B **73**, 064505 (2006).
[25] M. J. M. de Jong and C. W. J. Beenakker, Phys. Rev. Lett. **74**, 1657 (1995).
[26] M. Giroud, H. Courtois, K. Hasselbach, D. Mailly, and B. Pannetier, Phys. Rev. B **58**, R11872 (1998).
[27] I. Žutić and O. T. Valls, Phys. Rev. B **61**, 1555 (2000).
[28] G. J. Strijkers, Y. Ji, F. Y. Yang, C. L. Chien, and J. M. Byers, Phys. Rev. B **63**, 104510 (2001).
[29] J. N. Kupferschmidt and P. W. Brouwer, Phys. Rev. B **83**, 014512 (2011).
[30] A. F. Andreev, Sov. Phys. JETP **19**, 1228 (1964).
[31] V. V. Ryazanov, V. A. Oboznov, A. Yu. Rusanov, A. V. Veretennikov, A. A. Golubov, and J. Aarts, Phys. Rev. Lett. **86**, 2427 (2001).
[32] T. Kontos, M. Aprili, J. Lesueur, F. Genet, B. Stephanidis, and R. Boursier, Phys. Rev. Lett. **89**, 137007 (2002).
[33] J. W. A. Robinson, S. Piano, G. Burnell, C. Bell, and M. G. Blamire, Phys. Rev. B **76**, 094522 (2007).
[34] B. Kastening, D. K. Morr, L. Alff, and K. Bennemann, Phys. Rev. B **79**, 144508 (2009).

[35]D. Beckmann, H. B. Weber, and H. v. Löhneysen, Phys. Rev. Lett. **93**, 197003 (2004).
[36]P. S. Luo, T. Crozes, B. Gilles, S. Rajauria, B. Pannetier, and H. Courtois, Phys. Rev. B **79**, 140508(R) (2009).
[37]M. Colci, Ph.D. thesis, University of Illinois at Urbana-Champaign, 2010.
[38]M. Colci, K. Sun, N. Shah, S. Vishveshwara, and D. J. Van Harlingen, Phys. Rev. B **85**, 180512(R) (2012).
[39]T. Yamashita, S. Takahashi, and S. Maekawa, Phys. Rev. B **68**, 174504 (2003).
[40]J. Aarts, J. M. E. Geers, E. Bruck, A. A. Golubov, and R. Coehoorn, Phys. Rev. B **56**, 2779 (1997).
[41]J. Y. Gu, C.-Y. You, J. S. Jiang, J. Pearson, Y. B. Bazaliy, and S. D. Bader, Phys. Rev. Lett. **89**, 267001 (2002).
[42]F. Giazotto, F. Taddei, F. Beltram, and R. Fazio, Phys. Rev. Lett. **97**, 087001 (2006).
[43]M. Tian, N. Kumar, S. Xu, J. Wang, J. S. Kurtz, and M. H. W. Chan, Phys. Rev. Lett. **95**, 076802 (2005).
[44]F. Altomare, A. M. Chang, M. R. Melloch, Y. Hong, and C. W. Tu, Phys. Rev. Lett. **97**, 017001 (2006).
[45]T. Tokuyasu, J. A. Sauls, and D. Rainer, Phys. Rev. B **38**, 8823 (1988).
[46]F. Taddei and R. Fazio, Phys. Rev. B **65**, 134522 (2002).
[47]M. Tinkham, *Introduction to Superconductivity* (McGraw-Hill, New York, 1996).
[48]A. J. Leggett, *Quantum Liquids* (Oxford University Press, Oxford, 2006).
[49]A. F. Volkov, F. S. Bergeret, and K. B. Efetov, Phys. Rev. Lett. **90**, 117006 (2003).
[50]R. S. Keizer, S. T. B. Goennenwein, T. M. Klapwijk, G. Miao, G. Xiao, and A. Gupta, Nature (London) **439**, 825 (2006).
[51]M. Eschrig and T. Lofwander, Nat. Phys. **4**, 138 (2008).
[52]J. Linder, M. Cuoco, and A. Sudbo, Phys. Rev. B **81**, 174526 (2010).
[53]B. Almog, S. Hacohen-Gourgy, A. Tsukernik, and G. Deutscher, Phys. Rev. B **84**, 054514 (2011).
[54]M. D. Stiles, J. Appl. Phys. **79**, 5805 (1996).
[55]K. M. Schep, J. B. A. N. van Hoof, P. J. Kelly, G. E. W. Bauer, and J. E. Inglesfield, Phys. Rev. B **56**, 10805 (1997).
[56]K. Xia, P. J. Kelly, G. E. W. Bauer, and I. Turek, Phys. Rev. Lett. **89**, 166603 (2002).